Steel and Composite Structures, *Vol. 20, No. 4 (2016) 931-950*
DOI: http://dx.doi.org/10.12989/scs.2016.20.4.931

Effect of local wall thinning on ratcheting behavior of pressurized 90° elbow pipe under reversed bending using finite element analysis

Xiaohui Chen *[1,2] and Xu Chen [2a]

[1] *School of Control Engineering, Northeastern University, Qinhuangdao 066004, China*
[2] *School of Chemical Engineering and Technology, Tianjin University, 300072, China*

(*Received April 05, 2015, Revised December 18, 2015, Accepted January 06, 2016*)

Abstract. Ratcheting deformation of pressurized Z2CND18.12N stainless steel 90° elbow pipe with local wall thinning subjected to constant internal pressure and reversed bending was studied using finite element analysis. Chen-Jiao-Kim (CJK) kinematic hardening model, which was used to simulate ratcheting behavior of pressurized 90° elbow pipe with local wall thinning at extrados, flanks and intrados, was implemented into finite element software ANSYS. The local wall thinning was located at extrados, flanks and intrados of 90° elbow pipe, whose geometry was rectangular cross-section. The effect of depth, axial length and circumferential angle of local wall thinning at extrados, flanks and intrados on the ratcheting behaviors of 90° elbow pipe were studied in this paper. Three-dimensional elastic-plastic analysis with Chen-Jiao-Kim (CJK) kinematic hardening model was carried out to evaluate structural ratcheting behaviors. The results indicated that ratcheting strain was generated mainly along the hoop direction, while axial ratcheting strain was relatively small.

Keywords: FEA; constitutive model; elbow pipe; ratcheting effect; local wall thinning; ANSYS

1. Introduction

When subjected to internal pressure and cyclic loading, pipelines may face progressive deformation, so-called ratcheting effect. The ratcheting effect has been considered in several standards, such as ASME (2007), KTA (1995) and RCC-MR (1985). Aged pipings of nuclear power plants may have defects such as stress corrosion cracking and local thinning. Local wall thinning due to flow-accelerated corrosion was the main degradation mechanism of carbon steel piping components in nuclear power plants. Local wall thinning reduced the failure pressure, load-carrying capacity, deformation ability, and fatigue resistance of piping components. Therefore, it is important to evaluate ratcheting behavior of pressurized piping with local wall thinning in order to maintain the safety of the piping systems.

The wall thinning induced by corrosion was exacerbated at elbows because of stress concentration. Some researchers had studied low cyclic fatigue of elbows with local wall thinning (Kim *et al*. 2009, Takahashi *et al*. 2010). However, the ratcheting behavior of elbows with local

*Corresponding author, Ph.D., E-mail: chenxh@neuq.edu.cn
[a] Professor, E-mail: xchen@tju.edu.cn

 ISSN: 1229-9367 (Print), 1598-6233 (Online)

wall thinning was not yet clear. A lot of experiments on ratcheting deformation topic of pressurized elbow under cyclic bending focused on the sound elbow. Chen *et al*. (2013) presented an overview of recent progresses in experimental investigation and finite element analysis (FEA) of ratcheting behavior of pressurized piping. Based on experimental and FEA research, ratcheting boundaries have been determined with the final aim of aiding the safety design and assessment of engineering piping structures. The number of experiments on the ratcheting behavior of pressurized pipes was limited because these experiments were expensive, laborious, and time consuming. It was preferable to establish finite element method to simulate the experimental procedure. Vishnuvardhan *et al*. (2013) studied ratcheting deformation of Type 304LN stainless elbows subjected to steady internal pressure and cyclic bending. Results indicated that ratcheting strain occurred in the hoop direction at intrados, flanks and at a few other locations other than the extrados. No significant ratcheting strain was observed in both the axial and circumferential directions at the extrados location for all the specimens. It was also found that the elbows failed by the occurrence of through-wall axial crack in the curved portion, at one of the flank locations, accompanied by simultaneous bulging. Li *et al*. (2013) investigated the ratcheting and fatigue behavior of 90° single unreinforced mitred pipe bends subjected to constant internal pressure and a cyclic in-plane closing moment with a non-zero mean value. Both experiments and finite element analysis were used in that study. It was found that the main cause of mitre failure was ratcheting-fatigue interaction with the low cycle fatigue. Chen *et al*. (2015) studied the ratcheting behavior of pressurized straight pipe made of Z2CND18.12 austenitic stainless steel under loading control and displacement control conditions. Finite element analysis was adopted to predict ratcheting strain of straight pipe. Results found that CJK model showed reasonable simulation. Hassan *et al*. (2015) studied low-cycle fatigue and ratcheting responses of SS 304L 90 deg long-radius elbows subjected to repeated reversal force or displacement loading through experimental and analytical methods. It was indicated that all elbow specimens tested had failed by axial crack at flanks. Finally, Hassan *et al*. (2015) proposed that the scholars are still far from clearly understanding elbow failure responses.

Ratcheting behavior of structures has been simulated using the commercial finite element code ANSYS. The plasticity models with bilinear, multilinear and Chaboche kinematic hardening rule (Chaboche *et al*. 1979, Chaboche 1986) are currently available in the ANSYS code. The advanced plasticity models with modified Chaboche (Chaboche 1986, Chaboche *et al*. 1979), Ohno-Wang (1993a, b), Abdel Karim-Ohno (Abdel Karim and Ohno 2000) and modified Ohno-Wang (Chen *et al*. 2005) kinematic hardening rules were customized with ANSYS9.0 through the option of user programmable features. Shi *et al*. (2013) studied ratcheting deformation in elbow pipe made of Z2CND18.12N stainless steel with local wall thinning subjected to constant internal pressure and reversed in-plane bending under loading control. Three-dimensional elastic-plastic analyses using ANSYS incorporated with Chaboche and Chen-Jiao-Kim (CJK) kinematic hardening models were carried out to evaluate structural ratcheting behaviors.

In this paper, ratcheting behavior of pressurized 90° elbow pipe of Z2CND18.12N austenitic stainless steel with local wall thinning subjected to reversed bending was studied. The local wall thinning was located at inside and outside wall of 90° elbow pipe at extrados, flanks and intrados. Modified Ohno-Wang model (CJK model) was implemented into ANSYS by means of Euler backward scheme, implicit stress integration algorithm and Newton-Raphson iteration. Ratcheting simulation was performed by elastic-plastic finite element analyses with ANSYS where modified Ohno-Wang model (CJK model) was applied. The effect of geometric dimensioning such as depth, axial length and circumferential angle of local inside and outside wall thinning on the ratcheting

behavior of 90° elbow at extrados, flanks and intrados was indicated respectively.

2. Finite element model implementation

2.1 Finite element model implementation of advanced constitutive model

Constitutive model defined the material stress-strain relationship in finite element analysis. The rate independent plasticity models considered in this study share the following common features:

(1) von-Mises yield criterion (yield surface)

$$f = \left[\frac{3}{2}(\mathbf{s}-\boldsymbol{\alpha}):(\mathbf{s}-\boldsymbol{\alpha})\right]^{1/2} - \sigma_y = 0 \tag{1}$$

(2) Strain decomposition

$$d\varepsilon = d\varepsilon^e + d\varepsilon^p \tag{2}$$

$$d\varepsilon^e = \frac{1+v}{E}d\sigma - \frac{v}{E}tr(d\sigma)I \qquad \text{or} \qquad \sigma = D:\varepsilon^e \tag{3}$$

(3) Flow rule

$$\dot{\boldsymbol{\varepsilon}}^p = \dot{\lambda}\frac{\partial f}{\partial \boldsymbol{\sigma}} \tag{4}$$

where σ was the stress tensor, ε^e was the elastic strain tensor, ε^p was the plastic strain tensor, s was the deviatoric stress tensor, α was the current center of the yield surface in total stress space, σ_y was the size of the yield surface, v was the poisson's ratio, E was the elastic modulus and λ was plastic multiplier which was determined by consistent condition. The plastic multiplier λ was replaced by accumulated plastic strain rate p which was expressed in the following.

$$\dot{p} = \left(\frac{2}{3}\dot{\boldsymbol{\varepsilon}}^p : \dot{\boldsymbol{\varepsilon}}^p\right)^{1/2} \tag{5}$$

Eq. (1) was derived, and then substitution it into Eq. (4) provides

$$\dot{\boldsymbol{\varepsilon}}^p = \sqrt{\frac{3}{2}}\,\dot{p}\,N \tag{6}$$

where

$$N = \sqrt{\frac{3}{2}}\frac{\mathbf{s}-\boldsymbol{\alpha}}{\sigma_y} \tag{7}$$

N was the normal direction of yield surface which gave the direction plastic flow.
Substitution of Eq. (7) into Eq. (6) provided

$$\dot{\boldsymbol{\varepsilon}}^{p} = \frac{3}{2} \dot{p} \frac{\mathbf{s}-\boldsymbol{\alpha}}{\sigma_y} \tag{8}$$

(4) With the von-Mises yield criterion, the most important feature of a plasticity model in simulating ratcheting responses was the kinematic hardening rule, which determinesd the back stress increment

$$d\alpha = f\left(\sigma, \varepsilon^{p}, \alpha, d\sigma, d\varepsilon^{p}, \cdots\cdots\right) \tag{9}$$

A kinematic hardening rule dictated the translation of the yield surface during plastic loading and thereby influencing non-linear stress-strain and ratcheting responses.

2.2 Kinematic hardening rule

Chen *et al*. (2005) proposed a modified Ohno-Wang model for multiaxial ratcheting simulation (Abbr. CJK model), which stated as follows

$$d\alpha = \sum_{i=1}^{M} d\alpha_i \tag{10}$$

$$d\alpha_i = \gamma_i \left[\frac{2}{3} r_i d\varepsilon_p - \left\langle n' : \frac{\alpha_i}{\overline{\alpha_i}} \right\rangle \left(\frac{\overline{\alpha_i}}{r_i} \right)^{m_i} \alpha_i \left\langle d\varepsilon_p : \frac{\alpha_i}{\overline{\alpha_i}} \right\rangle \right] \tag{11}$$

where χ_i was a multiaxial parameter, $n' = \frac{d\varepsilon^{p}}{dp} = \frac{3}{2\sigma_y}(s-\alpha)$, the value of $\left\langle n' : \frac{\alpha_i}{\overline{\alpha_i}} \right\rangle$ was less than one in non-proportional loading and $\left\langle n' : \frac{\alpha_i}{\overline{\alpha_i}} \right\rangle^{\chi_i}$ was expected to take into account the non-proportional loading effects on ratcheting.

2.3 Application of radial return method

Simo and Taylor (1985, 1986) proposed tangent line which was used to predict radial return mapping, as shown in Fig. 1. The material was assumed as isotropic deformation and plastic incompressibility. Euler backward scheme combined with implicit integration algorithm was applied to updating stress of rate independent constitutive model. The relevant algorithm was given in the algorithm flowchart. The description of constitutive model of austenitic stainless steel ZCCND18.12N was studied in the paper.

2.3.1 Euler backward scheme

For each strain increment, the function of Euler backward scheme was that all state variables at the current n moment can be updated to the next $n+1$ moment, as expressed in the following

$$(\boldsymbol{\sigma}_n, \boldsymbol{\alpha}_n^{(i)}, \boldsymbol{\varepsilon}_n, \boldsymbol{\varepsilon}_n^{p}, p_n) \xrightarrow{\Delta\boldsymbol{\varepsilon}_{n+1}} (\boldsymbol{\sigma}_{n+1}, \boldsymbol{\alpha}_{n+1}^{(i)}, \boldsymbol{\varepsilon}_{n+1}, \boldsymbol{\varepsilon}_{n+1}^{p}, p_{n+1}) \tag{12}$$

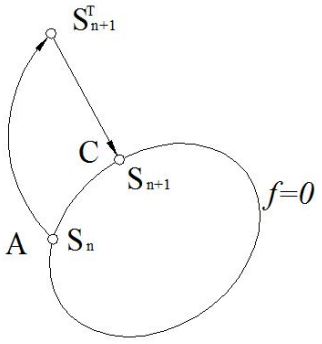

Fig. 1 Sketch of radial return mapping

Discrete version of Eqs. (1)~(11) was expressed as in the following

$$\boldsymbol{\varepsilon}_{n+1} = \boldsymbol{\varepsilon}^{e}_{n+1} + \boldsymbol{\varepsilon}^{p}_{n+1} \tag{13}$$

$$\boldsymbol{\sigma}_{n+1} = \mathbf{C} : \boldsymbol{\varepsilon}^{e}_{n+1} \tag{14}$$

$$\Delta\boldsymbol{\varepsilon}^{p}_{n+1} = \sqrt{\frac{3}{2}}\Delta p_{n+1}\mathbf{N}_{n+1} \tag{15}$$

$$\mathbf{N}_{n+1} = \sqrt{\frac{3}{2}}\frac{\mathbf{s}_{n+1} - \boldsymbol{\alpha}_{n+1}}{\sigma_y} \tag{16}$$

$$\Delta\boldsymbol{\varepsilon}^{p}_{n+1} = \frac{3}{2}\Delta p_{n+1}\frac{\mathbf{s}_{n+1} - \boldsymbol{\alpha}_{n+1}}{\sigma_y} \tag{17}$$

$$\boldsymbol{\alpha}_{n+1} = \sum_{1}^{M}\boldsymbol{\alpha}^{(i)}_{n+1} \tag{18}$$

$$f_{n+1} = \sqrt{\frac{3}{2}(\mathbf{s}_{n+1} - \boldsymbol{\alpha}_{n+1}) : (\mathbf{s}_{n+1} - \boldsymbol{\alpha}_{n+1})} - \sigma_y = 0 \tag{19}$$

Total strain increment $\Delta\varepsilon_{n+1}$ was assumed as elastic strain. Trial stress σ^{trial}_{n+1} was obtained by convergence solution σ_n when $t = t_n$.

$$\begin{aligned}\boldsymbol{\sigma}^{trial}_{n+1} &= \boldsymbol{\sigma}_n + \mathbf{C} : \Delta\boldsymbol{\varepsilon}_{n+1} = \mathbf{C} : [(\boldsymbol{\varepsilon}_n - \boldsymbol{\varepsilon}^{p}_n) + \Delta\boldsymbol{\varepsilon}_{n+1}] \\ &= \mathbf{C} : [(\boldsymbol{\varepsilon}_{n+1} - \boldsymbol{\varepsilon}^{p}_{n+1}) + \Delta\boldsymbol{\varepsilon}^{p}_{n+1}] = \boldsymbol{\sigma}_{n+1} + \mathbf{C} : \Delta\boldsymbol{\varepsilon}^{p}_{n+1}\end{aligned} \tag{20}$$

where, $\mathbf{C}$: $\Delta\varepsilon_{n+1}$ and $\mathbf{C}$: $\Delta\varepsilon^{p}_{n+1}$ represented respectively predicted stress increment and plastic correction term. According to isotropy hypothesis and plastic incompressibility, Eq. (21) was

obtained

$$\mathbf{C}:\Delta\boldsymbol{\varepsilon}_{n+1}^{p}=2G\Delta\boldsymbol{\varepsilon}_{n+1}^{p} \tag{21}$$

where G was shear elastic modulus, namely

$$G=\frac{E}{2(1+v)} \tag{22}$$

According to Eqs. (20)-(22), the relationship of stress tensor and deviatoric stress tensor was considered simultaneously. Deviatoric stress tensor can be written as

$$\mathbf{s}_{n+1}=\mathbf{s}_{n+1}^{trail}-2G\Delta\boldsymbol{\varepsilon}_{n+1}^{p} \tag{23}$$

In order to simplify expression form of CJK model, $\overset{\bullet}{p}^{(i)}$, which was assumed as the preceding part of dynamic recovery term, was written as

- CJK model

$$\overset{\bullet}{p}^{(i)}=\left(\frac{\bar{\boldsymbol{\alpha}}^{(i)}}{r^{(i)}}\right)^{m^{(i)}}\left\langle \overset{\bullet}{\boldsymbol{\varepsilon}}^{\mathrm{p}}:\frac{\boldsymbol{\alpha}^{(i)}}{\bar{\boldsymbol{\alpha}}^{(i)}}\right\rangle \tag{24}$$

- Critical state

$$f^{(i)}=\bar{\boldsymbol{\alpha}}^{(i)}-r^{(i)} \tag{25}$$

According to Eq. (24), evolutionary relationship of back stress of CJK model can be written as

$$\overset{\bullet}{\boldsymbol{\alpha}}^{(i)}=h^{(i)}\left[\frac{2}{3}\overset{\bullet}{\boldsymbol{\varepsilon}}^{\mathrm{p}}-\overset{\bullet}{p}^{(i)}\frac{\boldsymbol{\alpha}^{(i)}}{r^{(i)}}\right] \tag{26}$$

If $\zeta^{(i)}=\dfrac{h^{(i)}}{r^{(i)}}$, the Unified format of Eq. (24) can be expressed as

$$\boldsymbol{\alpha}=\sum_{i=1}^{M}\boldsymbol{\alpha}^{(i)},\qquad \overset{\bullet}{\boldsymbol{\alpha}}^{(i)}=\frac{2}{3}h^{(i)}\overset{\bullet}{\boldsymbol{\varepsilon}}^{\mathrm{p}}-\zeta^{(i)}\overset{\bullet}{p}^{(i)}\boldsymbol{\alpha}^{(i)} \tag{27}$$

Eq. (27) was to discretize, as expressed in the following

$$\boldsymbol{\alpha}_{n+1}^{(i)}=\theta_{n+1}^{(i)}\left(\boldsymbol{\alpha}_{n}^{(i)}+\frac{2}{3}h^{(i)}\Delta\boldsymbol{\varepsilon}_{n+1}^{p}\right) \tag{28}$$

where

$$\theta_{n+1}^{(i)}=\frac{1}{1+\zeta^{(i)}\Delta p_{n+1}^{(i)}} \tag{29}$$

Eq. (29) should satisfy $0<\theta_{n+1}^{(i)}\le 1$.

$\Delta p_{n+1}^{(i)}$ was expressed by the discrete version of Eq. (24), as shown in the following.

- CJK model

$$\Delta p_{n+1}^{(i)} = \left(\frac{\bar{\boldsymbol{\alpha}}_{n+1}^{(i)}}{r^{(i)}} \right)^{m^{(i)}} \left\langle \Delta \boldsymbol{\varepsilon}_{n+1}^{p} : \frac{\boldsymbol{\alpha}_{n+1}^{(i)}}{\bar{\boldsymbol{\alpha}}_{n+1}^{(i)}} \right\rangle \tag{30}$$

- Critical state

$$f_{n+1}^{(i)} = \bar{\boldsymbol{\alpha}}_{n+1}^{(i)} - r^{(i)} \tag{31}$$

Combined with Eqs. (18), (23) and (28) provided

$$\mathbf{s}_{n+1} - \boldsymbol{\alpha}_{n+1} = \mathbf{s}_{n+1}^{trail} - 2G\Delta \boldsymbol{\varepsilon}_{n+1}^{p} - \sum_{i=1}^{M} \theta_{n+1}^{(i)} (\boldsymbol{\alpha}_{n}^{(i)} + \frac{2}{3} h^{(i)} \Delta \boldsymbol{\varepsilon}_{n+1}^{p}) \tag{32}$$

Substitution of Eq. (17) into Eq. (32) provided

$$\mathbf{s}_{n+1} - \boldsymbol{\alpha}_{n+1} = \frac{\sigma_y (\mathbf{s}_{n+1}^{trail} - \sum_{i=1}^{M} \theta_{n+1}^{(i)} \boldsymbol{\alpha}_{n}^{(i)})}{\sigma_y + 3G\Delta p_{n+1} + \sum_{i=1}^{M} \theta_{n+1}^{(i)} h^{(i)} \Delta p_{n+1}} \tag{33}$$

According to Eq. (19) consistency condition was

$$\Delta p_{n+1} = \frac{[\frac{3}{2} (\mathbf{s}_{n+1}^{trail} - \sum_{i=1}^{M} \theta_{n+1}^{(i)} \boldsymbol{\alpha}_{n}^{(i)}) : (\mathbf{s}_{n+1}^{trail} - \sum_{i=1}^{M} \theta_{n+1}^{(i)} \boldsymbol{\alpha}_{n}^{(i)})]^{1/2} - \sigma_y}{3G + \sum_{i=1}^{M} \theta_{n+1}^{(i)} h^{(i)}} \tag{34}$$

Plasticity multiplier was obtained from the above nonlinear algebraic equation which was solved by Newton-Raphson iteration. Moreover, all internal variables at n+1 moment were obtained. The detailed algorithm flow was given in Fig. 2.

(1) Firstly, strain increment could be updated according to given the conditions.
(2) Strain increment was assumed as elastic strain, trial stress was obtained from Hooke's law. Considering yield condition Eq. (1), if $F < 0$ that the algebraic process could go back to the first step, otherwise, the third step.
(3) If $\theta_{n+1}^{(i)} = 1$, Δp_{n+1} obtained from Eq. (34), Eq. (35) was used to update $\mathbf{s}_{n+1} - \boldsymbol{\alpha}_{n+1}$

Eq. (16) was applied to updating $\mathbf{N}_{n+1}$, Eq. (15) was used to update $\Delta \varepsilon_{n+1}^{p}$, and Eq. (28) was applied to $\boldsymbol{\alpha}_{n+1}^{(i)}$, $\bar{\boldsymbol{\alpha}}_{n+1}^{(i)}$ ($\bar{\boldsymbol{\alpha}}_{n+1}^{(i)} = \sqrt{3/2 \boldsymbol{\alpha}_{n+1}^{(i)} : \boldsymbol{\alpha}_{n+1}^{(i)}}$), $\boldsymbol{\alpha}_{n+1}$ was calculated from Eq. (18), $\Delta p_{n+1}^{(i)}$ was calculated from Eq. (28), and $\theta_{n+1}^{(i)}$ was applied to updating Eq. (29).

(4) From Eq. (34) $\theta_{n+1}^{(i)}$ was calculated, $\Delta p'_{n+1}$ was obtained. Comparison of $\Delta p'_{n+1}$ and Δp_{n+1}, if the difference between $\Delta p'_{n+1}$ and Δp_{n+1} was in the range of the allowable error, the values of all internal variables of third step were at n+1 moment.
(5) Whether total strain had achieved a set value. If not achieved, returned to the first step, otherwise enter into the next step.
(6) Terminator.

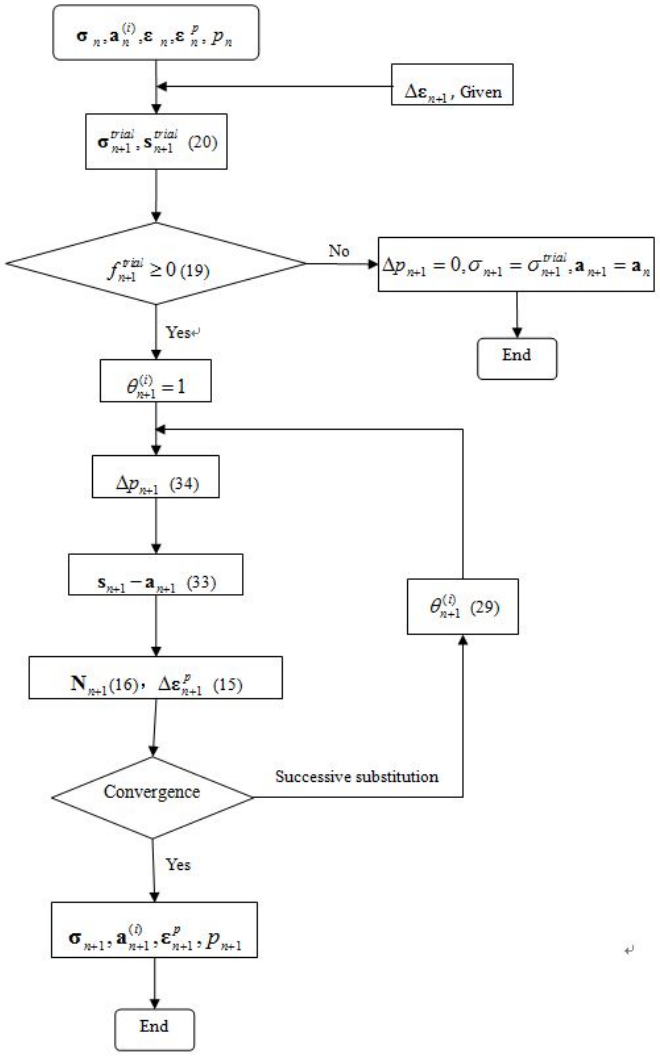

Fig. 2 Flowchart of radial return mapping algorithm for rate-independent model

2.3.2 Consistent tangent matrix

Algorithm modulus was used to determine trial strain increment of Newton-Raphson iteration, and then trial stress was determined. Therefore, algorithm modulus was calculated by local iteration carried out by radial return algorithm. According to Eq. (20), stress increment provided

$$\Delta\boldsymbol{\sigma} = \mathbf{C} : \Delta\boldsymbol{\varepsilon}^{\mathrm{e}} = \mathbf{C} : (\Delta\boldsymbol{\varepsilon} - \Delta\boldsymbol{\varepsilon}^{\mathrm{p}}) = \mathbf{C} : \left(\Delta\boldsymbol{\varepsilon} - \Delta\lambda \frac{\partial \mathrm{f}}{\partial \boldsymbol{\sigma}} \right) \tag{35}$$

General form of back stress increment was expressed as

$$\Delta\boldsymbol{\alpha} = -\mathrm{H}_{\mathrm{p}} \Delta\lambda \frac{\partial \mathrm{f}}{\partial \boldsymbol{\alpha}} = \mathrm{H}_{\mathrm{p}} \Delta\lambda \frac{\partial \mathrm{f}}{\partial \boldsymbol{\sigma}} \tag{36}$$

where H_p was plastic modulus. The above two equations was derived as

$$\mathrm{d}\boldsymbol{\sigma} = \mathbf{C} : \left[\mathrm{d}\boldsymbol{\varepsilon} - \mathrm{d}\lambda \frac{\partial \mathrm{f}}{\partial \boldsymbol{\sigma}} - \Delta\lambda \frac{\partial^2 \mathrm{f}}{\partial \boldsymbol{\sigma}^2} : \left(\mathrm{d}\boldsymbol{\sigma} - \mathrm{d}\boldsymbol{\alpha} \right) \right] \tag{37}$$

$$\mathrm{d}\boldsymbol{\alpha} = \mathrm{H_p} \mathrm{d}\lambda \frac{\partial \mathrm{f}}{\partial \boldsymbol{\sigma}} + \mathrm{H_p} \Delta\lambda \frac{\partial^2 \mathrm{f}}{\partial \boldsymbol{\sigma}^2} : (\mathrm{d}\boldsymbol{\sigma} - \mathrm{d}\boldsymbol{\alpha}) \tag{38}$$

Further, Eqs. (37) and (38) was combined

$$\left(\mathbf{C}^{-1} + \Delta\lambda \frac{\partial^2 \mathrm{f}}{\partial \boldsymbol{\sigma}^2} \right) : \mathrm{d}\boldsymbol{\sigma} - \Delta\lambda \frac{\partial^2 \mathrm{f}}{\partial \boldsymbol{\sigma}^2} : \mathrm{d}\boldsymbol{\alpha} = \mathrm{d}\boldsymbol{\varepsilon} - \mathrm{d}\lambda \frac{\partial \mathrm{f}}{\partial \boldsymbol{\sigma}} \tag{39}$$

$$-\Delta\lambda \frac{\partial^2 \mathrm{f}}{\partial \boldsymbol{\sigma}^2} : \mathrm{d}\boldsymbol{\sigma} + \left(\mathrm{H_p^{-1}} \mathbf{I} + \Delta\lambda \frac{\partial^2 \mathrm{f}}{\partial \boldsymbol{\sigma}^2} \right) : \mathrm{d}\boldsymbol{\alpha} = \mathrm{d}\lambda \frac{\partial \mathrm{f}}{\partial \boldsymbol{\sigma}} \tag{40}$$

If $\mathbf{A}^{-1} = \begin{bmatrix} \mathbf{C}^{-1} + \Delta\lambda \dfrac{\partial^2 \mathrm{f}}{\partial \boldsymbol{\sigma}^2} & -\Delta\lambda \dfrac{\partial^2 \mathrm{f}}{\partial \boldsymbol{\sigma}^2} \\ \Delta\lambda \dfrac{\partial^2 \mathrm{f}}{\partial \boldsymbol{\sigma}^2} & -\mathrm{H_p^{-1}} \mathbf{I} - \Delta\lambda \dfrac{\partial^2 \mathrm{f}}{\partial \boldsymbol{\sigma}^2} \end{bmatrix}$, Eqs. (39) and (40) was expressed as

$$\begin{bmatrix} \mathrm{d}\boldsymbol{\sigma} \\ \mathrm{d}\boldsymbol{\alpha} \end{bmatrix} = \mathbf{A} : \begin{bmatrix} \mathrm{d}\boldsymbol{\varepsilon} \\ 0 \end{bmatrix} - \mathrm{d}\lambda \mathbf{A} : \begin{bmatrix} \dfrac{\partial \mathrm{f}}{\partial \boldsymbol{\sigma}} \\ \dfrac{\partial \mathrm{f}}{\partial \boldsymbol{\sigma}} \end{bmatrix} \tag{41}$$

Consistent tangent condition was derived as

$$\mathrm{df} = \frac{\partial \mathrm{f}}{\partial \boldsymbol{\sigma}} : (\mathrm{d}\boldsymbol{\sigma} - \mathrm{d}\boldsymbol{\alpha}) = 0 \tag{42}$$

Substitution of Eq. (41) into Eq. (42) provided

$$\mathrm{df} = \left[\frac{\partial f}{\partial \boldsymbol{\sigma}}, \frac{\partial \mathrm{f}}{\partial \boldsymbol{\sigma}} \right] : \mathbf{A} : \begin{bmatrix} \mathrm{d}\boldsymbol{\varepsilon} \\ 0 \end{bmatrix} - \mathrm{d}\lambda \left[\frac{\partial \mathrm{f}}{\partial \boldsymbol{\sigma}}, \frac{\partial \mathrm{f}}{\partial \boldsymbol{\sigma}} \right] : \mathbf{A} : \begin{bmatrix} \dfrac{\partial \mathrm{f}}{\partial \boldsymbol{\sigma}} \\ \dfrac{\partial \mathrm{f}}{\partial \boldsymbol{\sigma}} \end{bmatrix} = 0 \tag{43}$$

If $\tilde{f} = \left[\dfrac{\partial \mathrm{f}}{\partial \boldsymbol{\sigma}}, \dfrac{\partial \mathrm{f}}{\partial \boldsymbol{\sigma}} \right]$, $\tilde{\mathbf{r}} = \begin{bmatrix} \dfrac{\partial \mathrm{f}}{\partial \boldsymbol{\sigma}} \\ \dfrac{\partial \mathrm{f}}{\partial \boldsymbol{\sigma}} \end{bmatrix}$, $\mathrm{d}\lambda$ in the Eq. (43) can be expressed as

$$\mathrm{d}\lambda = \frac{\tilde{f} : \mathbf{A}}{\tilde{f} : \mathbf{A} : \tilde{\mathbf{r}}} : \begin{bmatrix} \mathrm{d}\boldsymbol{\varepsilon} \\ 0 \end{bmatrix} \tag{44}$$

Substitution of Eq. (44) into Eq. (41) provided

$$\begin{bmatrix} \mathrm{d}\boldsymbol{\sigma} \\ \mathrm{d}\boldsymbol{\alpha} \end{bmatrix} = \left[\mathbf{A} - \frac{(\mathbf{A} : \tilde{\mathbf{r}}) \otimes (\tilde{f} : \mathbf{A})}{\tilde{f} : \mathbf{A} : \tilde{\mathbf{r}}} \right] : \begin{bmatrix} \mathrm{d}\boldsymbol{\varepsilon} \\ 0 \end{bmatrix} \tag{45}$$

where $\otimes$ represented tensor product. Eq. (45) was called as the general type of consistent tangent matrix of plasticity constitutive model.

2.4 Determination of material parameters

The parameters of the modified Ohno-Wang model (2015) were determined from uniaxial hysteresis loop, uniaxial and ratcheting experiments of straight pipe of Z2CND18.12N austenitic stainless steel, according to the method in reference (2000). The parameters γ_i and r_i were determined through the stress- strain curve of uniaxial tension test, as shown in Figs. 3(a) and (c).

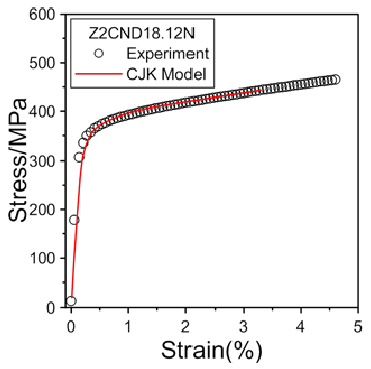

(a) Uniaxial tension

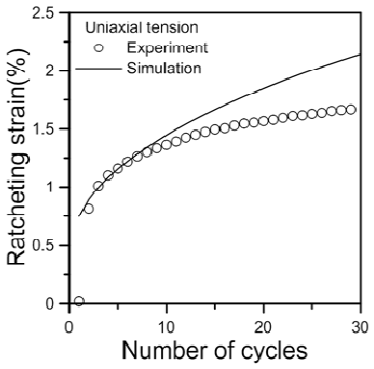

(b) Uniaxial ratcheting strain

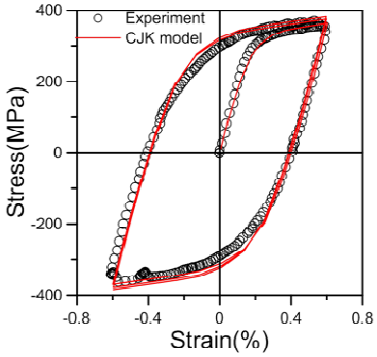

(c) Strain cycles

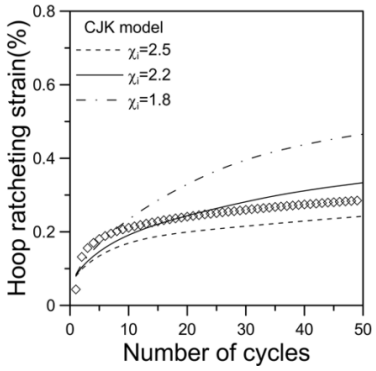

(d) Ratcheting strain of elbow pipe

Fig. 3 Simulation of ratcheting strain of straight pipe by CJK model

We thought that kinematic hardening rule was piecewise linearity. The more the piecewise number M of kinematic hardening rule, the closer stress-strain curve simulated than that of actual experimental data. For easier implementation, the piecewise number M should not be too many. In this study, the piecewise number M was six. The parameters γ_i and r_i were determined through the following equations

$$\gamma_i = \frac{1}{\varepsilon^{p(i)}} \tag{46}$$

$$r_i = \left(\frac{\sigma^{(i)} - \sigma^{(i-1)}}{\varepsilon^{p(i)} - \varepsilon^{p(i-1)}} - \frac{\sigma^{(i+1)} - \sigma^{(i)}}{\varepsilon^{p(i+1)} - \varepsilon^{p(i)}} \right) \varepsilon^{p(i)}, \; i = 1, 2 \cdots, M \tag{47}$$

where $\sigma^{(i)}$ and $\varepsilon^{(i)}$ represented respectively stress and strain in the ith piecewise point, $\sigma^{(i-1)}$ and $\varepsilon^{(i-1)}$ represented respectively stress and strain in the $(i-1)$th piecewise point, $\sigma^{(i+1)}$ and $\varepsilon^{(i+1)}$ represented respectively stress and strain in the $(i+1)$th piecewise point. Moreover, the parameter m_i was determined by the number of cycles -ratcheting strain curve of uniaxial ratcheting test, as shown in Fig. 3(b). These parameters were σ_y = 100 MPa, M = 6, C_1 = 400000 MPa, γ_1 = 8000, C_2 = 42000 MPa, γ_2 = 4000, C_3 = 124000 MPa, γ_3 = 2000, C_4 = 10000 MPa, γ_4 = 500, C_5 = 4200 MPa, γ_5 = 150, C_6 = 2200 MPa, γ_6 = 20, m_i = 4.5.

Note that only six decomposed rules were used for simulating the material responses. The material simulations with the determined parameters were shown in Fig. 3. The multiaxial parameter χ_i was determined by elbow pipe experiments (shown in Fig. 3(d)).

3. Structural simulation

3.1 Geometric model

Ratcheting behavior of sound pressurized 90° elbow pipe subjected to reversed in-plane bending under force controlled was studied in the paper. The outer diameter and thickness of the elbow pipe were 76 mm and 4.5 mm, respectively. The sketch of 90° elbow pipe apparatus was

(a) Sketch of specimen (b) Setup of experiment apparatus (c) Gauges distribution

Fig. 4 Sketch of 90° elbow pipe apparatus

shown in Fig. 4. Ratcheting deformation of pressurized 90° elbow pipe with local wall thinning subjected to reversed in-plane bending under force controlled was studied Local wall thinning occurred at inside and outside wall of 90° elbow pipe at extrados, flanks and intrados. According to the symmetry of structure and loading conditions, ratcheting strains at extrados, flanks and intrados (Fig. 4(c)) were mainly studied in this paper.

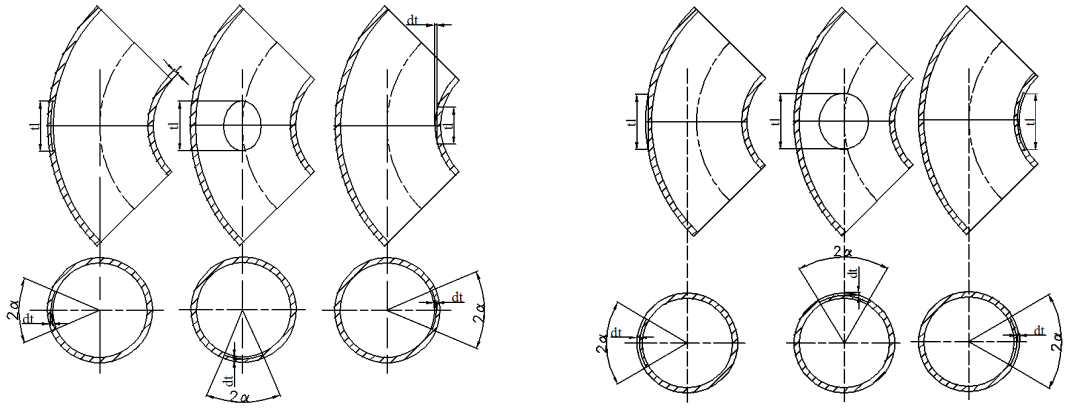

(a) Inside surface (b) Outside surface

Fig. 5 Schematic illustrations of 90° elbow with local wall thinning at extrados, flanks and intrados

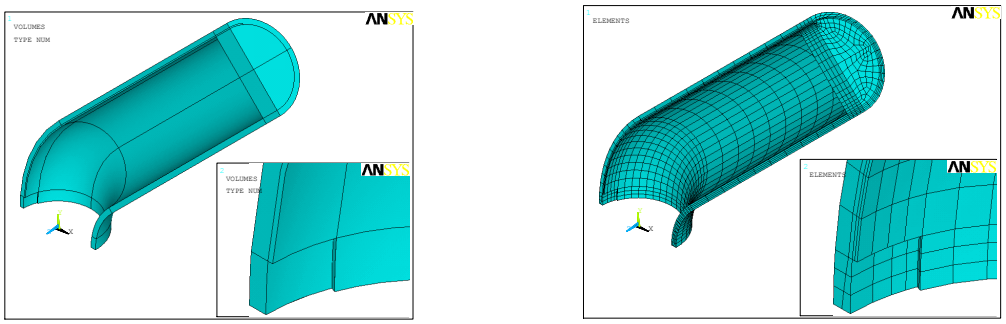

(a) Local wall thinning at outside surface at extrados

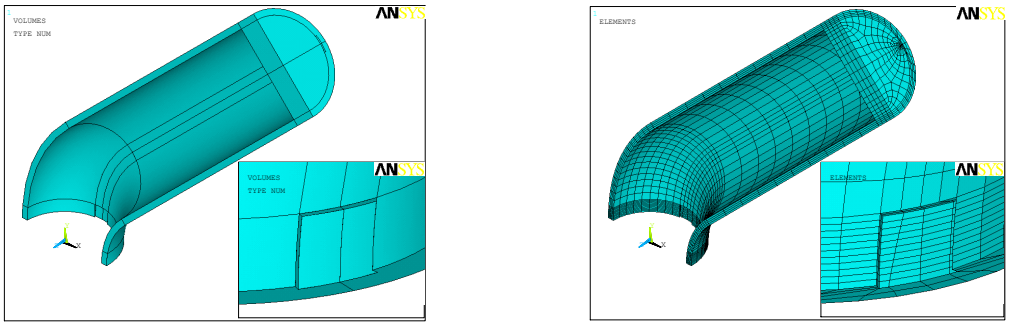

(b) Local wall thinning of inside surface at flank

Fig. 6 Finite element model and meshing of 90° elbow pipe with local wall thinning

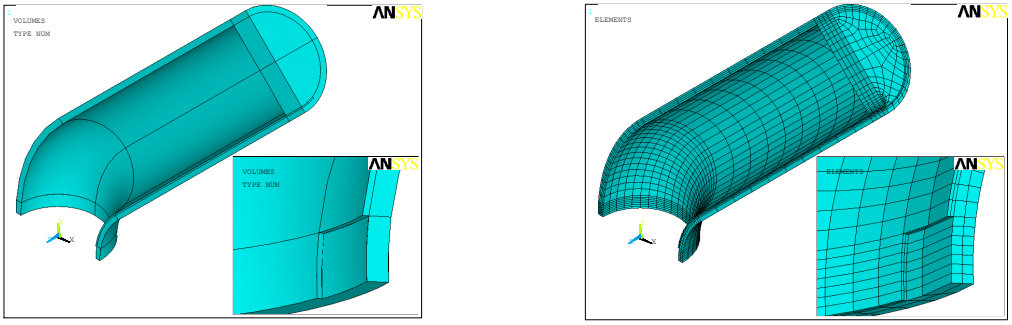

(c) Local wall thinning of inside surface at intrados

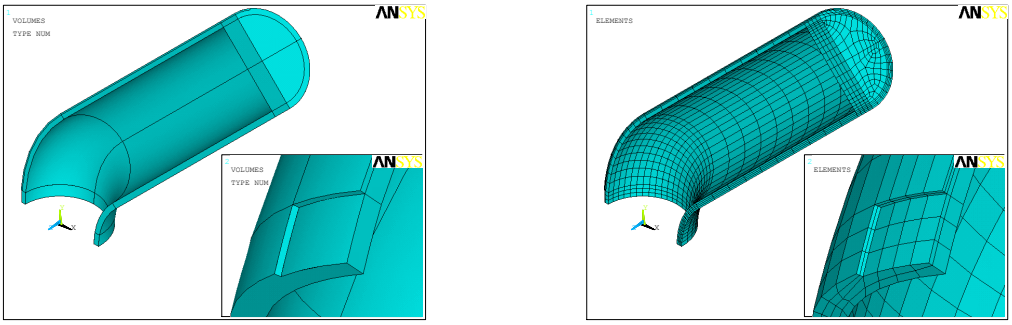

(d) Local wall thinning of outside surface at extrados

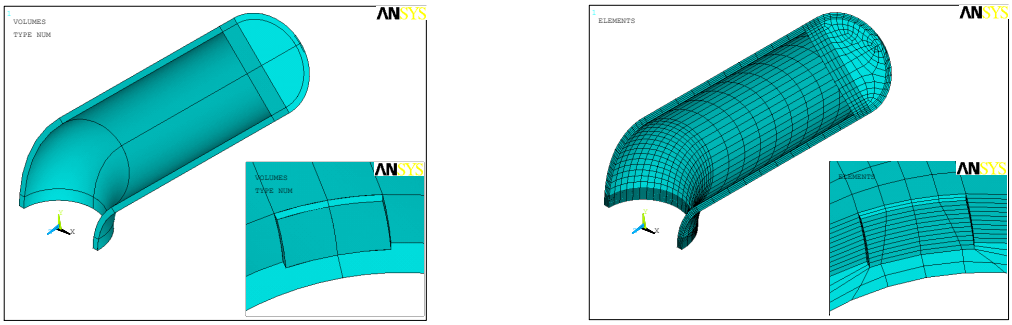

(e) Local wall thinning of outside surface at flank

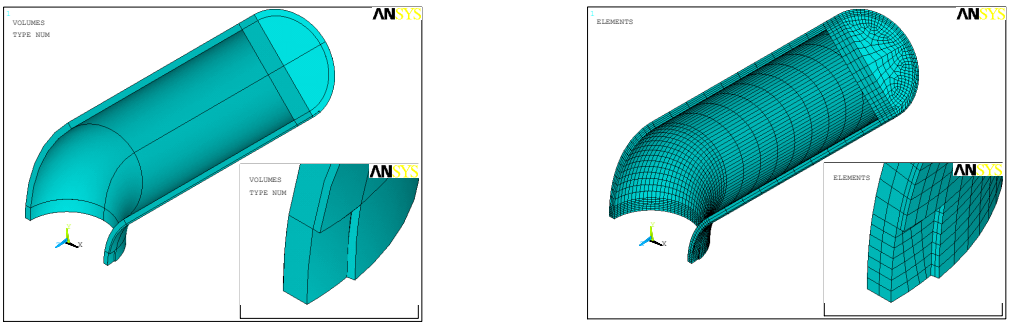

(f) Local wall thinning of outside surface at intrados

Fig. 6 Continued

3.2 Finite element model

3.2.1 Finite element model

Fig. 5 showed the schematic diagram of geometric dimensioning of 90° elbow pipe with local wall thinning. According to Figs. 5 and 4, finite element model and mesh of 90° elbow pipe with local inside and outside wall thinning at extrados, flanks and intrados was constructed by ANSYS software, as given in Fig. 6. Element type Solid45 in ANSYS and sweep mesh were used in the paper. A quarter of the structure was established due to symmetry of the 90° elbow pipe and loading conditions. In addition to the symmetric displacement constraints, internal pressure was applied to the inside surface of the pipe and end plate. In-plane reversed bending load was carried out by means of force controlled. Concentrated loading was applied in the in the *y*-direction at the center of the end plate. Ratcheting behavior of 90° elbow pipe subjected to 17.5 Mpa internal pressure and 20 kN bending loading was studied in this paper.

3.2.2 Results and discussions

Fig. 7 shows equivalent plastic strain contour in the fiftieth cycles of 90° elbow pipe subjected to 17.5 MPa internal pressure and 20 kN bending loading. The dimensions of local outside wall thinning at intrados were 1mm in depth, 10mm in axial length and 20° in circumferential angle.

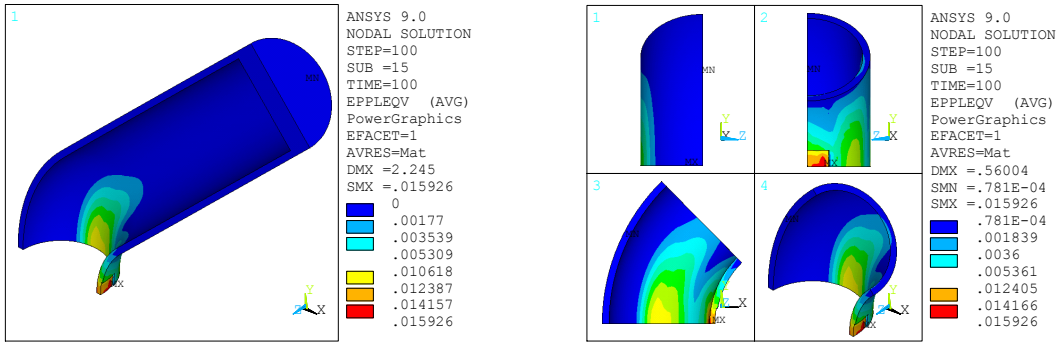

(a) (b)

Fig. 7 Equivalent plastic strain contour

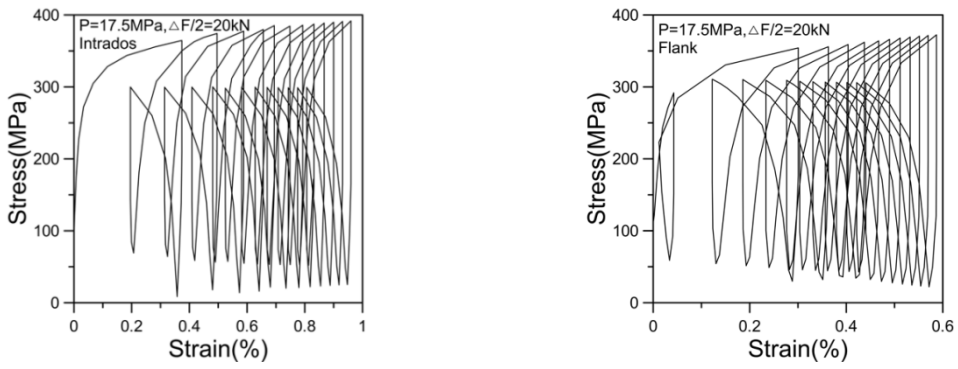

(a) At intrados (b) At flank

Fig. 8 Relationship between strain and stress

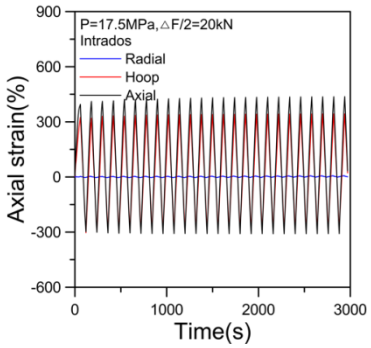

(a) Axial strain versus time

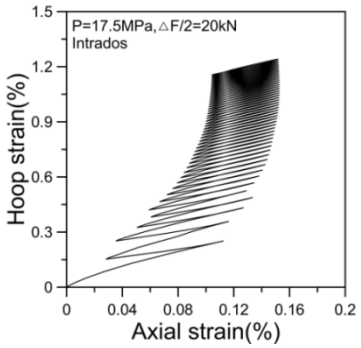

(b) Hoop strain versus axial strain

Fig. 9 The evaluation of axial and hoop strain

Stress concentration resulted from structural discontinuity of local wall thinning. Maximum accumulation plastic strain occurred at intrados, and ratcheting strain at flanks was relatively smaller.

Fig. 8 indicated the relationship of stress and strain at intrados and flanks. The relationship between timeand axial, radial and circumferential strain was shown in Fig. 9(a). Fig. 9(b) showed the curve of axial and circumferential ratcheting strain at intrados. It was found from Fig. 9 that the ratcheting strain was generated mainly in the axial and circumferential direction of 90° elbow pipe. The maximum ratcheting strain occurred in the circumferential direction of 90° elbow pipe, while axial ratcheting strain was relatively smaller and radial ratcheting strain the smalllest.

Fig. 10 shows the evolution law of axial, radial and circumferential direction ratcheting strain at flanks and intrados. It was found that ratcheting strain accumulation rate of axial and circumferential ratcheting strain was close to each other, and radial ratcheting strain was not prominent, as given in Fig. 10(a). Ratcheting strain of the above three directions at intrados was larger than that of flanks, which was attributed to local wall thinning at intrados of 90° elbow pipe. Ratcheting strain of inside and outside wall of intrados was compared in Fig. 10(b). It was found that circumferential ratcheting strain of inside wall at intrados was larger than that of outside wall, and axial and radial ratcheting strain of inside wall at intrados was smaller than that of outside wall.

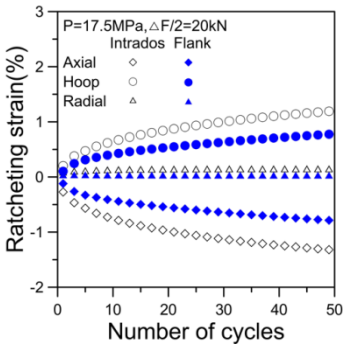

(a) At flank and intrados

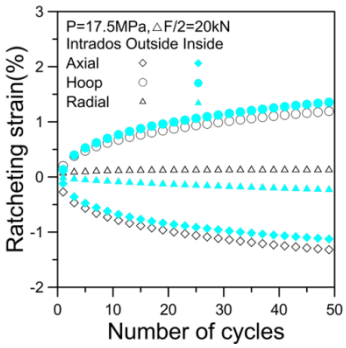

(b) At intrados

Fig. 10 Ratcheting strain

To sum up, the difference of ratcheting strain of inside and outside wall in the same direction was relatively small.

3.3 The effect of geometric dimensioning and position on ratcheting behavior of 90° elbow pipe

The effect of depth, axial length and circumferential angle of local wall thinning at extrados,

Table 1 Numerical matrix for 90° elbow pipe with local wall thinning

Num.	Depth *dt* (mm)	Axial length *tl*/2 (mm)	Circumferential angle α (°)	Positions (Flanks, intrados and extrados)
1	1	10	10	Inside/Outside Wall
2	2	10	10	Inside/Outside Wall
3	0.5/3.6	10	10	Inside/Outside Wall
4	1	10	10	Inside/Outside Wall
5	1	20	10	Inside/Outside Wall
6	1	40	10	Inside/Outside Wall
7	1	10	10	Inside/Outside Wall
8	1	10	20	Inside/Outside Wall
9	1	10	40	Inside/Outside Wall

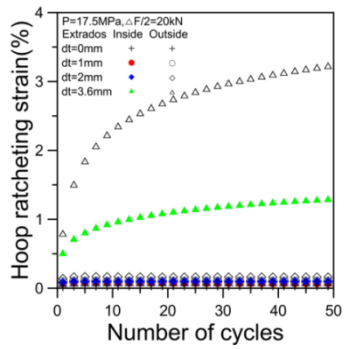

(a) At extrados

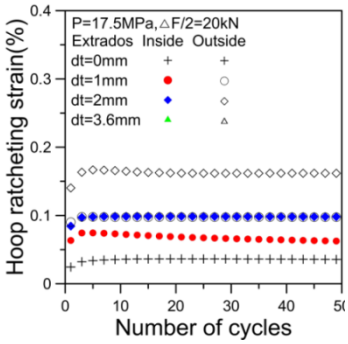

(b) Enlarged part at extrado

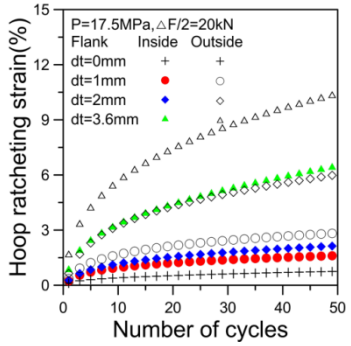

(c) At flank

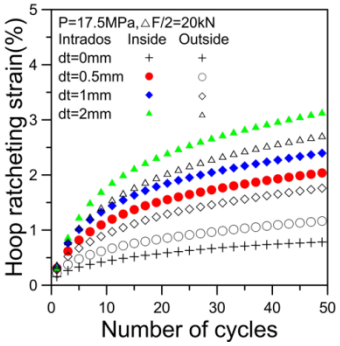

(d) At intrado

Fig. 11 Hoop ratcheting strain with different local wall thinning depth at different positions

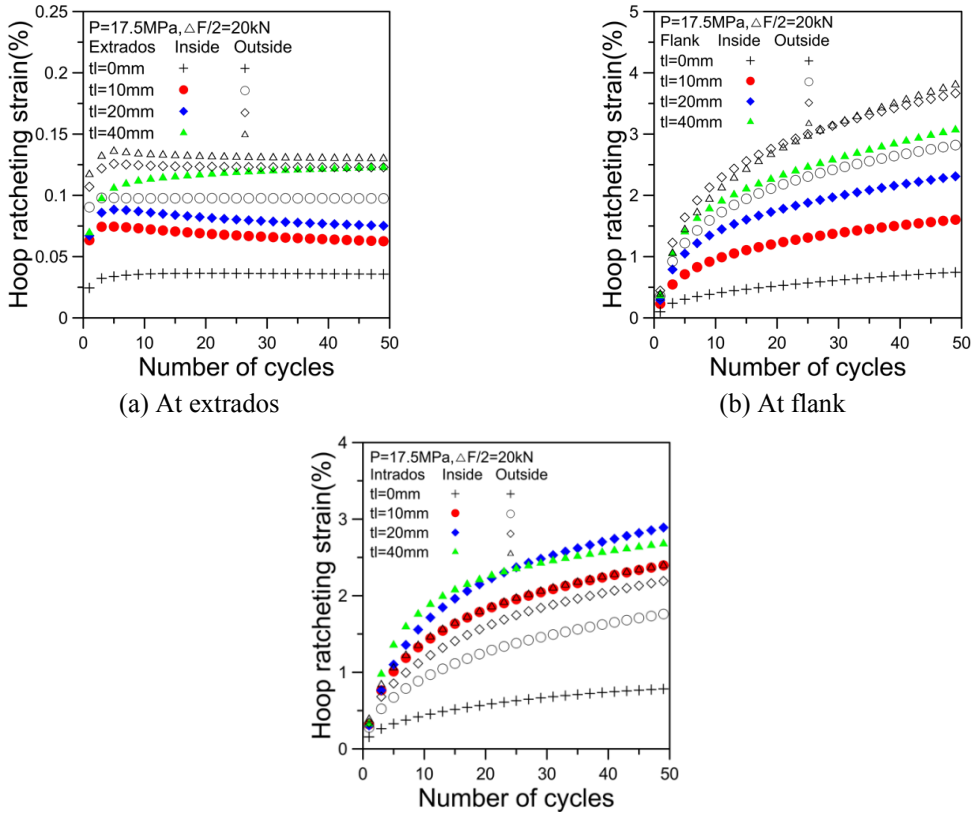

Fig. 12 Hoop ratcheting strain with different local wall thinning axial length at different positions

flanks and intrados on the ratcheting behavior of pressurized 90° elbow pipe subjected to reversed in-plane bending was also studied in the paper. The geometric dimensioning of local wall thinning was listed in Table 1.

3.3.1 The effect of depth on ratcheting behavior of 90° elbow pipe

The effect of different depth of local wall thinning on ratcheting strain of 90° elbow pipe was given in Fig. 11. The dimension with axial length of 10 mm and circumferential angle of 10° of local wall thinning was kept constant. Ratcheting strain of pressurized 90° elbow pipe with local inside or outside wall thinning under cyclic bending increased with the increasing of depth. The lower part of Fig. 11(a) was enlarged, which was shown in Fig. 11(b). For the same geometric dimensioning of local wall thinning at extrados and flanks, the effect of local outside wall thinning on ratcheting strain was larger than that of inside wall thinning, as shown in Figs. 11(a)-(c). Fig. 11(d) indicated that ratcheting strain at inside wall was larger than that of outside wall for pressurized 90° elbow pipe with local wall thinning under cyclic bending.

3.3.2 The effect of axial length on ratcheting behavior of 90° elbow pipe

Fig. 12 showed the effect of different axial lengths of local wall thinning on ratcheting strain of 90° elbow pipe with the depth of 1 mm and circumferential angle of 10° of local wall thinning kept

constant. In general, ratcheting strain of 90° elbow pipe with local inside or outside wall thinning increased with the increasing of axial length at extrados, flanks and intrados, as given in Figs. 12(a)-(c). The effect of axial length on ratcheting strain of 90° elbow pipe with local outside wall thinning was larger than that of inside wall at the same local wall thinning of flank and extrados. But Fig. 12(c) indicated that the effect of axial length on ratcheting strain of 90° elbow pipe with local inside wall thinning was larger than that of outside wall at intrados.

3.3.3 The effect of circumferential angle on ratcheting behavior of 90° elbow pipe

The effect of different circumferential angle of local wall thinning on ratcheting strain of 90° elbow pipe is shown in Fig. 13 with the axial length of 10 mm and depth of 1 mm of local wall thinning kept constant. Ratcheting strain of pressurized 90° elbow pipe with local inside or outside wall thinning under force controlled increased with the increasing of circumferential angle. For the same geometric dimensioning of local wall thinning, the effect of local outside wall thinning on ratcheting strain at extrados was smaller than that of inside wall thinning (Fig. 13(a)); the effect of local outside wall thinning on ratcheting strain at flanks was larger than that of inside wall thinning (Fig. 13(b)); the effect of local outside wall thinning with circumferential angle 10° on ratcheting strain at intrados was larger than that of inside wall thinning (Fig. 13(c)), and the effect of local outside wall thinning with circumferential angle 20° and 40° on ratcheting strain at intrados was smaller than that of inside wall thinning (Fig. 13(c)).

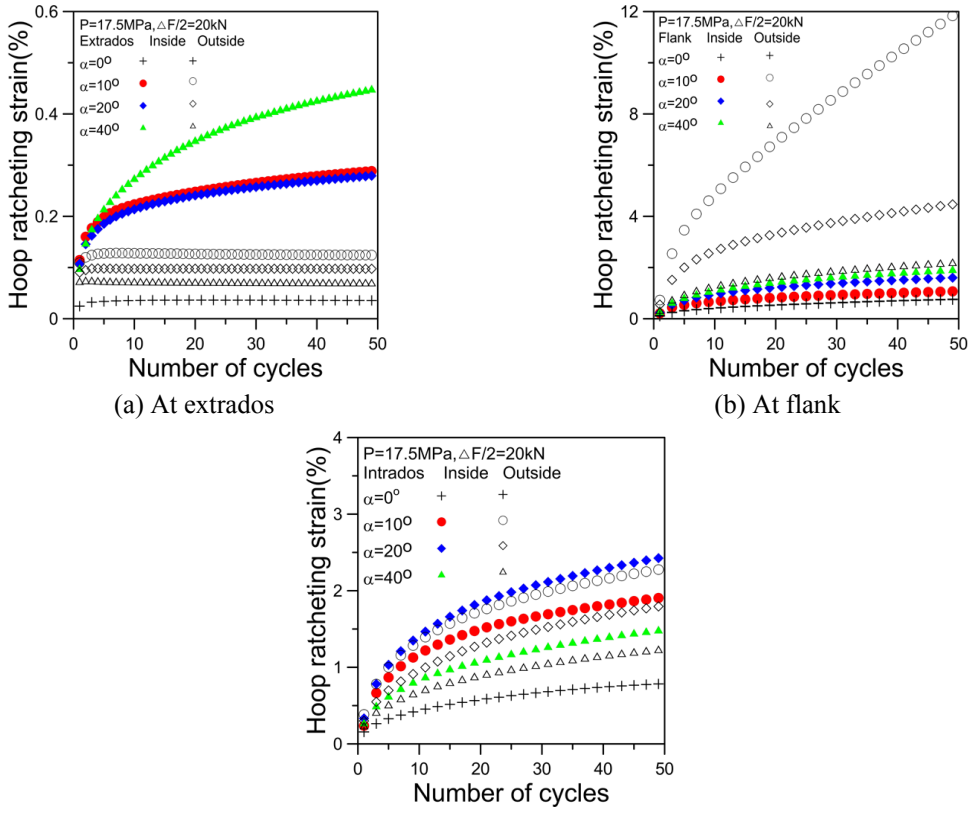

Fig. 13 Hoop ratcheting strain with different local wall thinning circumferential angle at different positions

4. Conclusions

Ratcheting behavior of pressurized 90° elbow pipe with local wall thinning subjected to in-plane reversed bending was studied by means of finite element analysis implemented with CJK model. Ratcheting strain of 90° elbow pipe with local inside or outside wall thinning at extrados, flanks and intrados were compared. In general, results indicated that for the same geometric dimensioning, the effect of local outside wall thinning on ratcheting strain at extrados and flanks was larger than that of inside wall thinning. It was just the opposite for that of intrados. Moreover, the effect of circumferential angle of local outside wall thinning on ratcheting strain at flanks was larger than that of inside wall. It was just the opposite for that of extrados and intrados. Not all ratcheting behavior of pressurized 90° elbow pipe subjected to in-plane reversed bending increased with the increasing of the size of local wall thinning at extrados, flanks and intrados.

Acknowledgments

The authors gratefully acknowledge financial support for this work from the Fundamental Research Funds for the Central Universities (XNB2015001), Youth Foundation of Hebei Educational committee (No. QN2015336), National Natural Science Foundation of China (No. 51435012) and Ph.D. Programs Foundation of Ministry of Education of China (No. 20130032110018).

References

Abdel Karim, M. and Ohno, N. (2000), "Kinematic hardening model suitable for ratcheting with steady-state", *Int. J. Plast.*, **16**(3-4), 225-240.

ASME (2007), American society of mechanical engineers; Section iii, New York, NY, USA.

Bari, S. and Hassan, T. (2000), "Anatomy of coupled constitutive model of ratcheting simulation", *Int. J. Plast.*, **16**(3-4), 381-409.

Bari, S. and Hassan, T. (2002), "An advancement in cyclic plasticity modeling for multiaxial ratcheting simulation", *Int. J. Plast.*, **18**(7), 873-894.

Chaboche, J.L. (1986), "Time independent constitutive theories for cyclic plasticity", *Int. J. Plast.*, **2**(2), 149-188.

Chaboche, J.L., Dang-Van, K. and Cordier, G. (1979), "Modelization of the strain memory effect on the cyclic hardening of 316 stainless steel", *Proceedings of the 5th International Conference on SMiRT*, Div. L, Berlin, Germany, August.

Chen, X., Jiao, R. and Kim, K.S. (2005), "On the Ohno-Wang kinematic hardening rules for multiaxial ratchetting modeling of medium carbon steel", *Int. J. Plast.*, **21**(1), 161-184.

Chen, X.H., Chen, X., Yu, D.J. and Gao, B.J. (2013), "Recent progresses in experimental investigation and finite element analysis of ratcheting in pressurized piping", *Int. J. Pres. Ves. Pip.*, **101**, 113-142.

Chen, X.H., Chen, X., Chen, G. and Li, D.M. (2015), "Ratcheting behavior of pressurized Z2CND18.12N stainless steel pipe under different control modes", *Steel Compos. Struct., Int. J.*, **18**(1), 29-50.

Hassan, T., Rahman, M. and Bari, S. (2015), "Low-cycle fatigue and ratcheting responses of elbow piping components", *J. Press. Vess. - T. ASME*, **137**(3), 031010-1-12.

Kim, J.W., Lee, S.H. and Park, C.Y. (2009), "Experimental evaluation of the effect of local wall thinning on the failure pressure of elbows", *Nucl. Eng. Des.*, **239**(12), 2737-2746.

KTA (1995), Kerntechnischer Ausschuß; Sicherheitstechnische Regel des KTA, Komponenten des primärkreises von Leichtisserreaktoren, Teil: Auslegung, Konstruktion und Berchnung, Regeländerung-sentwurf.

Li, H., Wood, J., McCormack, R. and Hamiton, R. (2013), "Numerical simulation of ratcheting and fatigue behavior of mitred pipe bends under in-plane bending and internal pressure", *Int. J. Pres. Ves. Pip.*, **101**, 154-160.

Ohno, N. and Wang, J.D. (1993a), "Kinematic hardening rules with critical state of dynamic recovery, Part I: formulations and basic features for ratcheting behavior", *Int. J. Plast.*, **9**(3), 375-390.

Ohno, N. and Wang, J.D. (1993b), "Kinimatic hardening rules with critical state of dynamic recovery, Part II: Application to experiments of ratcheting behavior", *Int. J. Plast.*, **9**(3), 391-403.

RCC-MR (1985), Design rules for class 1 equipment, RCC-MR codes, revision.

Shi, H.G., Chen, G., Wang, Y. and Chen, X. (2013), "Ratcheting behavior of pressurized elbow pipe with local wall thinning", *Int. J. Pres. Ves. Pip.*, **102-10**3, 14-23.

Simo, J.C. and Taylor, R.L. (1985), "Consistent tangent operators for rate-independent elastoplasticity", *Comput. Method. Appl. Mech. Eng.*, **48**(1), 101-118.

Simo, J.C. and Taylor, R.L. (1986), "A return mapping algorithm for plane stress elasto –plasticity", *Int. J. Numer. Meth. Eng.*, **22**, 649-670.

Takahashi, K., Tsunoi, S., Hara, T., Ueno, T., Mikami, A., Takada, H., Ando, K. and Shiratori, M. (2010), "Experimental study of low-cycle fatigue of pipe elbows with local wall thinning and life estimation using finite element analysis", *Int. J. Pres. Ves. Pip.*, **87**, 211-219.

Vishnuvardhan, S., Raghava, G., Gandhi, P., Goyal, S., Gupta, S.K. and Bhasin, V. (2013), "Ratcheting strain assessment in pressurized stainless steel elbows subjected to in-plane bending", *Procedia Eng.*, **55**, 666-670.

CC